Undrained cyclic response of K_0–consolidated stiff Cretaceous clay under wheel loading conditions

K Pan[1]; X M Liu[2]; Z X Yang, M.ASCE[3]; R J Jardine[4]; and Y Q Cai[5]

Abstract

Optimal whole life design for railways, highways, runways and metro lines requires accurate assessment of how their underlying geomaterials respond to large numbers of wheel–loading cycles. This paper presents an experimental study on a natural UK stiff clay with cyclic triaxial (CT) and hollow cylinder apparatus (CHCA) that imposed K_0 and wheel–loading stress conditions. The focus is on Gault clay, a high OCR marine clay deposited in the Cretaceous, whose mechanical behavior is significantly anisotropic and in-situ K_0 values exceed unity. The clay outcrops under sections of most major highways radiating out of London, as well as the HS1 and new HS2 high-speed railways. The experimental investigation explored how the principal stress rotation implicit in wheel loading increases the magnitudes and changes the sign of vertical strain accumulation, as well as accelerating resilient modulus degradation and accentuating stress–strain hysteresis, all of which affect pavement or rail-track serviceability. The clay's deformation and pore pressure responses are categorized into stable, metastable, and unstable patterns. Comparisons with related studies on

[1] Postdoctoral fellow, College of Civil Engineering, Zhejiang University of Technology, Hangzhou 310014, China. Email: pk2013@zju.edu.cn

[2] Postgraduate student, Department of Civil Engineering, Zhejiang University, Hangzhou 310058, China. Email: 21712019@zju.edu.cn

[3] Professor, Research Center of Coastal and Urban Geotechnical Engineering, Department of Civil Engineering, Zhejiang University, Hangzhou 310058, China (corresponding author). Email: zxyang@zju.edu.cn

[4] Professor, Department of Civil and Environmental Engineering, Imperial College London, London, UK. Email: r.jardine@imperial.ac.uk

[5] Professor, College of Civil Engineering, Zhejiang University of Technology, Hangzhou 310014, China. Email: caiyq@zju.edu.cn

low OCR, low K_0 soft clay from Wenzhou in southeastern China, confirm the Gault clay's generally stiffer pre-failure behavior and different cyclic response. The stiff clay's greater brittleness is also emphasized; particle re-orientation occurs readily along distinct shear bands, leading to dramatic shear strength reductions that have a major impact on slope and foundation stability and call for appropriate caution in practical design.

Key words: Stiff clay; cyclic wheel loading; principal stress rotation; strain accumulation; pore pressure

Introduction

Optimal whole-life design for transport infrastructure foundations requires accurate analysis of how long-term cyclic wheel loading generated by moving axle loads affects the deformation and resilient behavior of the underlying geomaterials (Puppala et al. 1999; Gu et al. 2012; Guo et al. 2013; Wang et al. 2013; Qian et al. 2019). Surface settlements are generally most critical for routes passing over clay terrains and assessment of the clays' response to undrained cyclic straining is an important first step in exploring the potential service settlements; further consideration of movements generated as pore pressures dissipate is required to complete the picture; Guo et al (2018). Cyclic triaxial (CT) tests provide one means of assessing the clay's cyclic response (Hyde et al. 1976; Yasuhara et al. 1982; Zhou and Gong 2001; Puppala et al. 2009). Numerous one-way CT test programs have been conducted to aid traffic loading analysis (see Monismith et al. 1975; Li and Selig 1996;

Chai and Miura 2002; or Xiao et al. 2014) as well as two-way CT laboratory studies (Shahu et al. 1999; Suiker et al. 2005) with symmetrical and/or asymmetrical cycling about the isotropic axis. The major (σ_1) and minor (σ_3) principal stresses undergo jump rotations when the isotropic axis is crossed, and the major and minor principal stresses are alternately axial or radial. CT programs have identified how different soils' cyclic responses are governed by their particulate make-up, initial states and cyclic stress conditions, and so aided the development of permanent accumulation models that consider the impacts of varying cyclic stress levels and load cycle numbers.

However, CT tests cannot capture important aspects of the undrained wheel–loading stress paths, which implicitly include cyclic principal stress axis rotation (PSR) caused by the wheels' application of horizontal shear stress cycles that accompany the alternating changes in vertical and horizontal normal stresses. To do this requires test equipment such as hollow cylinder apparatus (HCA) which can provide four degrees of freedom and vary the vertical (σ_z), radial (σ_r), circumferential (σ_θ), and shear ($\tau_{z\theta}$) stresses to apply independent control of the stress parameters (p', q, α, and b) defined as below

$$p' = \frac{\sigma_1' + \sigma_2' + \sigma_3'}{3} = \frac{\sigma_1 + \sigma_2 + \sigma_3}{3} - u \qquad (1)$$

$$q = \sqrt{\frac{1}{2}\left[\left(\sigma_1' - \sigma_2'\right)^2 + \left(\sigma_2' - \sigma_3'\right)^2 + \left(\sigma_3' - \sigma_1'\right)^2\right]} \qquad (2)$$

$$\alpha = \frac{1}{2}\tan^{-1}\left(\frac{2\tau_{z\theta}}{\sigma_z' - \sigma_\theta'}\right) \qquad (3)$$

$$b = \frac{\sigma_2' - \sigma_3'}{\sigma_1' - \sigma_3'} \quad (4)$$

where p' is effective mean principal stress, q is the generalized deviatoric stress, α is the orientation of the major principal stress axis relative to the vertical, b is the intermediate principal stress ratio, u is pore water pressure, and σ'_1, σ'_2 and σ'_3 are the effective major, intermediate, and minor principal stresses, respectively.

Hight et al. (1983), Towhata and Ishihara (1985), Zdravkovic and Jardine (1997), Nakata et al. (1998), Nishimura et al. (2007), Yang et al. (2007), Brosse et al. (2017a, b) and Qian et al. (2018), inter-alia, have shown that rotating α (PSR) has a marked influence on strain development, stiffness degradation, and pore pressure generation in soils under undrained conditions, even when all other factors are held constant. Cyclic HCA (CHCA) studies reported by Gräbe and Clayton (2009; 2014), Xiao et al. (2014) and Cai et al. (2015) involving isotropically consolidated samples verified that strain development is more severe with low OCR sediments than in equivalent CT tests when stress paths representing all the traffic loading components are applied. Wu et al. (2017), Cai et al. (2017) and Qian et al. (2018) argued that CHCA tests on anisotropically consolidated samples represent field conditions more faithfully and reported tests on low OCR sediments (with $K_0 = \sigma'_r/\sigma'_z < 1$) that show how incorporating PSR in CHCA tests leads to greater permanent vertical strain accumulation, especially when the deviatoric stress changes become large. CT or isotropic CHCA tests are likely to lead to non-conservative assessments for transport infrastructure founded in terrains such as the wide level areas of soft (low OCR, low

K_0) post-glacial (Holocene) clays encountered in southeastern China.

The question remains open, however, as to how the undrained imposition of wheel–loading stress paths might affect other types of clays, including the stiff, geologically-aged plastic high OCR clays that are found worldwide and cover approximately 50% of the southern UK (Wilkinson 2011). Much of the UK's transport links, such as expressways, rail lines, and airport runaways, have been built on such high OCR strata, within which the in-situ K_0 values generally exceed unity, leading to their initial σ_1 axes being oriented horizontally, rather than vertically, as is usual in low OCR soils.

This paper addresses the question by exploring in undrained CT and CHCA tests the cyclic response of a high OCR, stiff clay deposit from the UK. The examined Gault clay, which outcrops under sections of most major highways radiating out of London, as well as the HS1 and new HS2 high-speed railway lines, was deposited in the lower Cretaceous 99–112 million years ago and experienced monotonic loading as several hundred meters of other sediments built up after deposition. Unloading by erosion followed that led to the stratum's present shallow depth; Wilkinson (2011). Glacial and periglacial activity, forest growth and weathering followed that led to the profiles of properties reported for the Authors' sampling site by Hosseini Kamal et al. (2014) and Brosse et al. (2017a, b). As described later, their work assessed $K_0 \approx 1.8$ over the depth range of interest.

This study reports undrained CT and CHCA experiments on saturated intact samples re-consolidated to K_0 ≈ 1.8 insitu stresses before experiencing idealized undrained cyclic wheel loading stress paths that included PSR. The permanent strain, resilient stiffness and pore pressure characteristics are presented and analyzed before a unified interpretation is made to synthesize the observed responses. Comparisons with parallel studies on natural (low OCR, low K_0) Holocene soft clay from Wenzhou in SE China help identify the different trends associated with the far stiffer, older and higher OCR Gault clay.

Material and equipment

The Gault clay was sampled at High Cross, 3 km west of Cambridge, UK, at a site where the water table varies seasonally around an average depth ≈ 1 m below ground level; Hosseini Kamal et al. (2014). Two different sampling methods were employed. Careful block sampling to 3 m from a trench offered the best possible samples. Continuous, high-quality, wireline, triple-barrel, rotary sampling was also undertaken to 13 m depth in two boreholes with the Geobore 'S' system. The latter employed a natural polymer-based drilling mud to maintain borehole stability and alleviate the possibility of swelling of the clay due to the flush fluid. The cores extracted from the boreholes were immediately cleared of all drilling mud and softened material before being preserved in several layers of alternating plastic film and wax, with a final layer of aluminum foil, before being retained in the split plastic lining tubes and bubble wrap in strong core boxes and stored in a cool and humid environment. Hosseini-Kamal et al. (2014) showed that the two approaches both led to high-quality samples that gave similar outcomes in parallel triaxial tests conducted on specimens taken by both methods over similar depth ranges. Further check triaxial tests conducted several years at ZJUT later showed similar outcomes to the earlier Imperial College tests, demonstrating that the experiments described in this paper had not been affected unduly by the long storage times or careful air transport. The experiments reported in this paper concentrated on specimens prepared from block samples taken at 3m and rotary cores from 5.28 to 8.45 m depth. As illustrated in Table 1, the high plasticity, high OCR, Gault clay in-situ water contents fell around the plastic limits at both of the depths considered.

The blocks were taken from an area that had become covered by shrubs and trees whose roots had desiccated the clay at shallow depths and accelerated chemical weathering (Wilkinson 2011). Their micro-to-meso structures were investigated by Wilkinson (2011) and Hosseini Kamal (2012). The degree of biological (e.g., tree roots) and chemical (e.g., oxidation) weathering decreased with depth, with the Gault's colors darkening markedly below the weathered layers. Weathering affects the structure and mechanical behavior of the soil in different manners. Piezocone and Seismic Cone Penetration tests conducted by Hosseini Kamal (2012) indicated reduced CPT cone resistances and sleeve frictions in the weathered zone which were not evident below the base of the light-colored weathered clay. Weathering is interpreted as the main reason for the shallow samples' different response to undrained cycling. At the micro-scale, Wilkinson (2011) observed that weathering caused a major reduction in the degree of the Gault clay's preferred particle orientation while at the meso-scale the shallow samples were more intensively fissured.

Monotonic experiments conducted at Imperial College London (ICL)

The monotonic behavior of the Gault clay is illustrated in Fig. 1, which presents undrained triaxial compression test results by Hosseini Kamal (2012) on Gault clay samples from two depths (3.5 and 6.5 m) at the same sampling site. The shallower sample was sheared after isotropic re-consolidation (p'_0 = 70 kPa, q_0 = 0), while the deeper rotary sample was reconsolidated to its in-situ K_0 state (p'_0 = 125 kPa, q_0 = –60 kPa). Peak undrained shear strengths S_u of ≈ 70 and 120 kPa were found with the shallow-weathered and deep samples, respectively. While the pre-peak pore pressure changes shown in Fig. 1(b) were larger for the deeper sample, both tests show pore pressures declining post-peak due to the stiff clay's dilative tendency as it attempts to shear towards critical state conditions. Hosseini-Kamal (2012) terminated his deeper sample test after smaller strains for operational reasons, but both specimens bifurcated and started to develop shear discontinuities post peak. Large-displacement ring shear tests show that the Gault clay develops remarkably low residual angles of shearing resistance within such shear bands due to clay particle reorientation. Hosseini Kamal (2012) also noted higher compressibility and swelling coefficients in oedometer tests on his shallow-weathered samples. His results suggest yield stress ratios (YSRs) in the 25 to 37 range, which are lower than the OCRs inferred from the Gault clay's maximum past burial depth, reflecting the Gault's complex post-depositional geological history.

Table 2 lists the compressibility, triaxial critical state line, residual shear strength and other parameters determined in triaxial and ring-shear tests run at Imperial College London (ICL), after Hosseini Kamal et al. (2014), which confirmed the Gault clay's marked brittleness with residual ϕ'_r values that fall far below the clay's peak or critical state triaxial shear values. Low residual shear strengths impact slope and foundation stability and call for great caution in practical design.

Wilkinson (2011), Hosseini Kamal (2012) and Brosse (2012) confirmed that the Gault clay has significant structural anisotropy owing to its complex grain interactions and void distributions, as well as patterns of meso-scale discontinuities and fissures. Brosse (2012) found that the deep samples typically featured three sets of meso-scale discontinuities: one subvertical, one at approximately 45^{o} from the vertical, and the last at approximately 75^{o}. The discontinuity spacings were generally greater than 100 mm. The shallow-weathered Gault clay is more intensively fissured. Monotonic triaxial and HCA experiments by Brosse et al. (2017a, b) revealed significant strength and stiffness anisotropy for the Gault clay. Probing tests on samples from around 11 (+/- 1.5) m depth indicated E_h^U, E_v^U and G_{vh} maxima of 690, 132 and 57 MPa respectively; Brosse et al. (2017b).

Cyclic experiments run at Zhejiang University of Technology (ZJUT)

The CT tests run at ZJUT were conducted on 38 mm diameter, 76 mm high specimens with an advanced electromechanical Dynamic Triaxial Testing System (DYNTTS) with the servo-loading and signal conditioning systems detailed by Wang et al. (2013). CHCA tests were performed with dynamic hollow cylinder apparatus (DYNHCA) manufactured by GDS Instruments Ltd, which employs servomotors to control axial and torsional movements and can cycle stresses at frequencies up to 5 Hz. Digital controllers apply the back, inner, and outer cell pressures, through de-aired water systems. The measurement ranges and resolutions of the transducers are listed in Table 3; further apparatus details are given by Grabe and Clayton (2014), Cai et al. (2015) and Guo et al. (2017). The measurement systems inevitably suffer from a degree of apparatus compliance and their limited resolutions lead to “stepwise” trends at very small axial strains (< 0.005% in CT and < 0.001% for CHCA tests), as shown later. Such discontinuities dominate the torsional shear deformation observations when shear strain < 0.036%, and a smoothing routine was applied to help reduce their impact on the strain measurements. The CHCA specimens have 200 mm height (H) and outer and inner diameters (d_o and d_i) of 100 and 60 mm, giving d_i/d_o and H/d_o ratios of 0.6 and 2, respectively. While the degree of stress uniformity achieved in HCA specimens depends on their geometry and the platen arrangements, the degrees of variation appear tolerable for apparatus with the GDS CHCA’s d_i/d_o

and H/d_o ratios; Hight et al. (1983). The expressions summarized in Table 4 were employed to calculate the average specimen stresses and strains (Yang et al. 2007).

Test procedures

The CT and CHCA experiments run at ZJUT on natural samples of Gault clay employed similar preparation procedures to Hosseini Kamal et al. (2014) and Brosse et al. (2017a). Specimens were trimmed from cores or blocks to the specified d_o (approximately 38 and 100 mm in CT and CHCA tests, respectively) using a wire saw and a rigid knife in a rotary soil lathe. The CT tests on the shallow-weathered Gault clay relied on block samples with length, width, and height of 300, 300, and 300 mm, respectively, which were pre-divided by bandsaw into prismatic sections of appropriate dimensions before trimming to cylinders. The necessary inner cylindrical voids required for CHCA tests (on rotary samples) were formed by encasing the trimmed cylinders in a rigid mold and using a metal working lathe to achieve the desired d_i with minimal disturbance by advancing rotating drill bits of ascending outer diameter. After trimming the ends flat, the specimens were carefully installed with (external or internal/external) latex membranes over systems of surface filter paper drains. To ensure the application of sufficient traction during torsional shearing, the sharp edges of shear vanes were anchored into the CHCA sintered bronze vertical platens. Fully saturated specimens (with Skempton's B-values exceeding 0.95) were obtained by applying a back pressure of 600 kPa for 48 hours to dissolve gas bubbles as completely as possible. Maintaining high backpressure over the subsequent re-consolidation and creep stages ensured still higher final, pre-shearing, *B*-values.

Hosseini Kamal et al. (2014) and Brosse et al. (2017a) assessed a potential in-situ K_0 range 1.5 to 3.0 for the Gault clay by considering its high OCR values. However, a relatively low limiting K_0 of 1.8 was found necessary to avoid excessive straining of the specimens during triaxial reconsolidation stages, and this value was adopted as the most appropriate for the Authors' tests. Applying $K_0 = 1.8$ with the measured unit weights and water table depth led to in-situ effective stresses estimates of σ'_{z0} = 39 kPa, σ'_{r0} = 70 kPa and σ'_{z0} = 77 kPa, σ'_{r0} = 139 kPa respectively, for the shallow (3 m) and deep (7 m average) sample groups, as shown in Table 5.

Specimens were isotropically consolidated at a p' rate of 3 kPa/h from their initial states of suction (typically equal to 25 kPa, point A) before imposing (at either point B or D, depending on sample depth) a pause period of several days to allow for complete drainage and stabilization. Once the axial strain creep rates had reduced below $2 \cdot 10^{-3}$ %/h (as recommended by Brosse 2012), the specimens were extended under drained conditions, i.e., paths B→C and D→E depicted in Fig. 2. During this stage, σ'_r was increased at a rate of 2/3 kPa/h, while simultaneously decreasing σ'_z at –4/3 kPa/h to maintain constant p' while q deceased by 2 kPa/h. These stress conditions were maintained again until the axial creep strain rate fell below the $2 \cdot 10^{-3}$ %/h rate limit.

Schemes of undrained cyclic loading were then applied at 1 Hz, as suggested for traffic loading by Ishihara (1996) and Cai et al. (2017). The CT tests involved cycling vertical stresses sinusoidally from minima, representing in-situ σ'_{z0} stresses, to maxima of (σ'_{z0} + $\Delta\sigma'_z$), while the radial stress (σ'_{r0}) was held constant. The CHCA experiments varied both the vertical (σ'_z) and torsional shear ($\tau_{z\theta}$) stresses, following the mathematical expressions set out by Guo et al. (2018). The test data reported for one test in Fig. 3 demonstrate that the apparatus could represent idealized versions of the wheel–loading stress path closely. As shown in Fig. 3(a), σ'_z decreased to its minimum (point A) as $\tau_{z\theta}$ increased at the start of each cycle; then $\tau_{z\theta}$ was raised to the maximum (point B) before σ'_z reached its peak at point C, after which a $\tau_{z\theta}$ cycle was applied with the opposite sign, leading to a trough at point D as σ'_z crossed the minimum (point E) and finally returned to its initial value.

This idealized loading scheme matches numerical and experimental results from earlier pavement engineering studies (e.g., Brown 1996; Lekarp et al. 2000; Powrie et al. 2007; Ishikawa et al. 2011), which identified the cardioid incremental $2\tau_{z\theta}$–(σ'_z-σ'_θ) stress path shape shown in Fig. 3(b). Two key parameters defined below, the vertical cyclic stress ratio (VCSR) and η (the ratio between the maximum increments of torsional shear stress and vertical cyclic stress) were employed to characterize the test paths:

$$\mathrm{VCSR} = \Delta\sigma'_z / 2p'_0 \tag{5}$$

$$\eta = \Delta\tau_{z\theta} / \Delta\sigma'_z \tag{6}$$

where $\Delta\sigma'_z$ is the maximum increment of vertical cyclic stress and $\Delta\tau_{z\theta}$ is the maximum increment of torsional shear stress. The angle α varied according to Eq. (7) below.

$$\tan 2\alpha = \frac{2\tau_{z\theta}^{cyc}}{\sigma_z'^{cyc} + \sigma_{z0}' - \sigma_{\theta0}'} \quad (7)$$

The inner and outer cell pressures (p_i and p_o) were kept equal in CHCA, leading to $b = \sin^2(\alpha)$. Table 5 summarizes the combinations of parameters applied in 28 CT and CHCA tests, which are divided into three series based on the loading schemes and sample types. The tests on shallow-weathered and deep samples generally extended to 10,000 or 50,000 cycles respectively, unless they failed at earlier stages, as occurred in two CHCA experiments and one CT test. Cyclic failure was defined as occurring when either: i) the axial strains exceed 10% or ii) the strain rates become too high for the actuators to maintain the desired stress paths.

Test results and discussion

Fig. 4(a) and (b) illustrates the vertical (ε_z) and shear ($\gamma_{z\theta}$) strain components developed during an individual CHCA stress cycle. In Fig. 4(a), ε_z^t is the total vertical strain developed over loading while ε_z^r is the resilient vertical strain developed over unloading, and ε_z^p is the permanent vertical strain developed over single cycle. Similar rules applied to the $\gamma_{z\theta}$ strains as shown in Fig. 4(b). The onset of hysteretic stress-strain loops that open-up as permanent strains accumulate is taken as indicating a second form of kinematic yielding, which is termed Y_2 within the framework proposed by Jardine (1992).

Permanent strain accumulation

Fig. 5 presents the typical responses of deep samples under CT conditions when purely positive cycles of compressive vertical stress increments were applied. The vertical strains that are the primary cause of surface settlement remained small in the lowest VCSR CT tests and showed no significant tendency to accumulate as cycling continued. More significant compressive vertical strains developed in tests with VCSR > 0.2 that grew with increasing VCSR and tended to stabilize with N in tests involving moderate VCSRs. When imposed from K_0 = 1.8, the low VCSR cyclic stress paths tended to reduce the deviatoric stresses by loading vertically and led to stable outcomes. However, the application in higher VCSR tests of $\sigma'_z > \sigma'_r$ led to pore pressure build-up under cycling and gradually increasing effective stress t/s' ratios at each cyclic peak, and stress paths that headed towards compressive failure. Discontinuous steps were seen when shear bands developed in some (higher VCSR) cases, such as the VCSR = 0.6 case, which mobilized its first shear band at around N = 500, accompanied by sharp increase in ε_z accumulation. A second band appeared at approximately N = 18,600 showing similar phenomena. However, the pre-existing discontinuities required to enable such stepped patterns were not present in all specimens. The highest VCSR (0.699) case showed continuous (compressive) strain accumulation that decelerated towards a plateau with $\varepsilon_z \approx 6\%$ over the later stages of cycling.

Fig. 6 shows the equivalent vertical strain trends from four CHCA tests conducted on deep samples, employing varying VCSR values combined with constant η = 1/3. As illustrated in Fig. 3, the initial stage of each CHCA cycle involved σ'_z reductions, which led to the absolute (generalized) deviatoric stress rising and the effective stress points moving towards failure with α close to 90^o. Reductions in α followed as $\tau_{z\theta}$ increments were applied, which became more marked as σ_z reversed and grew to achieve its maximum. CHCA tests with VCSR greater than ≈ 0.25 led to $\sigma'_z > \sigma'_r$ and α rotating fully to 0^o at the right hand extreme of the stress cycle.

The CHCA stress conditions led to key differences with the CT tests. Strain accumulation became significant from lower VCSR values, as their paths involved deviatoric loading from the K_0 = 1.8 conditions towards extension failure. Consequently, the specimens tended to extend axially rather than compress and the first 'left hand' stages of the cardioid path (Fig. 3(b)) inflicted the greatest damage. In addition, stepped traces indicating shear band mobilization involving extension were seen at lower VCSRs than in the CT tests. There was also a less clear tendency for straining to stabilize with increasing N and the highest VCSR (0.450) case underwent full cyclic failure. The same points are shown by comparing the vertical strain trends of the CT and CHCA experiments directly in Fig. 7.

It might be argued that the different CT and CHCA trends might be artefacts of the apparatus employed or specimen size effects. However, Nishimura (2006), working another geologically aged, high K_0, stiff high OCR plastic UK (London) clay conducted identical tests in an HCA with comparable dimensions to the Authors' (inner/outer diameter of 38/76 mm) and triaxial cells. Intact (non-fissured) specimens of London clay from the same site and depth were sheared under η = 0 conditions from their in-situ stresses at b = 1 and good agreement was observed between the peak shear 'triaxial' strengths obtained in the different apparatuses. Hosseini Kamal et al. (2014) addressed specimen-size effects in detail for four stiff UK clays, relating these to their natural meso-structures of fissures and discontinuities. While important effects were noted in some cases, the Gault clay's particular meso-structure led to no clear trend between tests on specimens with 38, 50 and 100 mm diameters.

Some key observations relating to the effects on residual creep rates on vertical strain accumulation at lower VCSRs should be also be noted. The rate, $d\varepsilon_z^p/dN$, of vertical extension strain shown in Fig. 7(a) for a CHCA test with VCSR = 0.127 was broadly compatible with the residual (extensile) creep strain rate $d\varepsilon_z^p/dt$ tolerated before cycling started after consolidation with $\sigma'_r > \sigma'_z$ and added to any response to cycling. In contrast, the compressive straining developed in the equivalent CT test was counteracted by the specimen's residual extensile creep rate, leading to a negligible overall apparent $d\varepsilon_z^p/dN$ development.

The CHCA and CT tests' ε_z^p trends with VCSR and N are synthesized and illustrated in Fig. 8. Cai et al. (2017) and Guo et al. (2018) reported closely similar tests on soft, low

OCR, Wenzhou clay samples that were normally consolidated (with K_0 = 0.55) to achieve undrained triaxial shear strengths ≈ 25 kPa. In keeping with the jargon adopted by these authors, the Gault clay specimens manifested "stable", "metastable", or "unstable" responses. As shown in Fig. 8(a), any (extensive) ε_z^p strain accumulation in CHCA (η = 1/3) tests on deep samples appeared negligibly small until VCSR exceeded 0.15, the upper 'stable cyclic threshold' condition for Gault clay, which is comparable with the Y_2 yielding condition defined by Jardine (1992). Cycling above the Y_2 limit led to ε_z^p values (developed after fixed numbers of cycles N) that grew linearly with VCSR up to VCSR ≈ 0.35 with a "metastable" style of response that generated permanent strains, but no failure within 50,000 cycles. The growth of ε_z^p with respect to N becomes steeper at higher VCSRs, showing an "unstable" trend; shear bands developed in some cases and full cyclic failures occurred after numbers of cycles, N, that reduced with VCSR. The permanent shear strains $\gamma_{z\theta}^p$ determined in the CHCA tests conducted with η = 1/3 are synthesized and presented in Fig. 9, showing comparable trends with VCSR to the axial strains and similar stable-to-metastable and metastable-to-unstable region boundaries.

Significantly higher equivalent threshold VCSR values (0.23 and 0.55) are interpreted for the "stable" and "metastable" limits applying to the deep samples under CT (η = 0) loading, as shown in Fig. 8(b). Equally, raising η from 1/3 to 1/2 while keeping fixed VCSR leads to steeper rates of strain accumulation and earlier onsets of instability, as shown earlier in Fig. 7(b). However, as only one CHCA test with η = 1/2 was conducted in this study, the thresholds for the η = 1/2 case cannot be identified definitively. CT tests on the shallow-weathered Gault clay presented in Fig. 8(c) indicated marginally lower “stable” and “metastable” VCSR limits (0.2 and 0.5 respectively) than the deep samples, showing that desiccation and weathering rendered the Gault less resistant to cyclic loading.

The equivalent trends from Cai et al. (2017) and Guo et al’s (2018) CT tests on soft normally (K_0 = 0.55) consolidated Wenzhou clay are included in Fig. 8(c), showing distinctly lower threshold VCSRs than either the weathered or deeper Gault clay samples. Guo et al (2018) showed that still steeper rates of compressive vertical straining develop in CHCA tests on Wenzhou clay conducted at comparable VCSRs. The insensitive, stiff and geologically aged high OCR (high K_0) Gault clay has significantly greater cyclic resistance than the Holocene Wenzhou clay. However, the Gault clay extends rather than compresses in response to undrained wheel loading. It is also brittle and susceptible to developing very low shear strength on shear bands, a feature that was not seen with the Wenzhou clay.

Resilient stress–strain responses

The Gault clay’s monotonic stiffness response is highly anisotropic; Brosse et al. (2017b) and involves marked degradation with strain once its initial elastic limits is exceeded after very small strains. For the cyclic stress conditions considered herein, the stiffness represented by the vertical (M_z^r) and shear ($G_{z\theta}$) resilient moduli can be defined as the backbone curve slopes of the vertical and shear stress–strain hysteretic loops, as shown in Fig. 4(a) and (b), respectively. Under the test conditions considered the M_z^r modulus is directly comparable to the E_v^U moduli reported by Brosse et al. (2017b) and the $G_{z\theta}$ shear modulus to their G_{vh} stiffness. Fig. 10 shows the typical hysteretic responses of CT (η = 0) and CHCA (η = 1/3) tests conducted at the same VCSR (= 0.343) with the overall loops presented in Fig. 10(a) and (c) exhibiting the permanent strain trends, showing again the different strain signs and rates developed in the two tests series. The strain scales adopted in Fig. 10(b) and (d) have their strain origins re-zeroed at the specified cycle numbers (i.e., *N* = 1, 10, 100, 1,000, 10,000, and 50,000) to highlight changes in resilient moduli with increasing *N*, indicating again far steeper reductions in modulus with *N* in the CHCA experiments.

Fig. 11 compares the CT and CHCA tests conducted at VCSR = 0.343 further, adding the experiment with η = 1/2 and considering the ‘re-zeroed strain’ loops found after *N* = 10, 100, 1,000, and 10,000. The degree to which the near elliptical loops’ rotate clockwise as η and *N* increases reflects the degrees to which the cardioid paths lead to softer responses and accelerate stiffness degradation; the η = 1/2 case cannot be plotted in Fig. 11 (d) because it failed before *N* reached 2,500.

Fig. 12 reports more directly how M_z^r degrades with *N* in different test series, showing both engineering units and normalized ratios M_z^r/p'_0. The maximum stiffness observed, around 125 MPa, in the CT-I test at VCSR = 0.067 shown in Fig.

12(b) is compatible with, and only slightly lower than, the elastic E_v^U = 132 MPa reported by Brosse et al. (2017b) from very small strain, locally instrumented, triaxial probing tests on (slightly deeper) samples from ≈ 11 m depth. While progressively lower M_z^r values apply in the CT-I tests conducted at higher VCSRs, their degradation with increasing *N* remains relatively modest. The CT-II tests on shallow-weathered samples indicate lower absolute moduli in Fig. 12(c), but broadly comparable normalized M_z^r/p'_0 trends. While the CHCA test at VCSR = 0.067 (with η = 1/3) also shows M_z^r comparable to the elastic E_v^U = 132 MPa in Fig. 12(a), CHCA tests show much steeper decays of modulus with *N* than the equivalent CT tests.

Horizontal shear stress–strain hysteretic loops are shown in Fig. 13 for the *N* = 1, 10, 100, 1,000, 10,000, and 50,000 stages of four CHCA tests, which indicate stiff behavior at the lowest VCSR plotted, with neither hysteresis nor shear modulus degradation. The hysteretic loops open-up once Y_2 yielding develops, at the onset of metastable behavior. They also rotate clockwise as η and *N* increase at higher VCSRs. The variations of shear modulus $G_{z\theta}$ with respect to VCSR, η and *N* are presented directly in Fig. 14. The maximum $G_{z\theta}$ value found in the lowest VCSR (0.067) test appears independent of *N* and matches the elastic G_{vh} = 57 MPa value reported by Brosse et al. (2017b). The experiments confirm the marked reductions of non-linear shear stiffness with *N* and η that develops at the higher VCSR ratios.

Pore pressure development

The cyclic experiments demonstrate how excess pore pressure builds up during undrained cyclic loading after Y_2 yielding, in parallel with strain accumulation and stiffness degradation. Dissipation of pore pressures after cycling leads to volume changes and further strains that make important contributions to the settlement of pavements or rail-tracks in service; Guo et al (2018). Fig. 15 presents the cyclic pore pressure increments developed in CT tests on deep samples, normalized by the initial mean effective stress as $\Delta r_u = u/p'_0$ and plotted against N, identifying also the ratios Δr_u^p found from the permanent pore pressures applying at the end of each stress cycle. While the lowest VCSR (0.088) test shows a stable trend for pore pressures to remain constant with N, tests involving higher VCSRs show initial increases in pore pressures that appeared to stabilize as N grew, with the Δr_u^p ratios growing systematically with VCSR.

The equivalent CHCA plots presented in Fig. 16 confirm negligible Δr_u^p at low VCSR (0.067) and values that increase systematically with increasing VCSR until failures start to develop on shear bands. High OCR clays attempt to dilate as they shear to large strains and Figs. 16(c) and (d) show how this feature led to Δr_u^p dipping in tests that were progressing to unstable outcomes.

The CHCA and CT tests' Δr_u^p ratios are synthesized and plotted against VCSR in Fig. 17, revealing again the three styles of response noted for strain development in Figs. 8 and 9. Stable response patterns in pore pressure generation can also be observed at low VCSRs that change to indicate metastable trends above the indicated threshold ratios. However, the unstable CHCA tests indicate less systematic changes than the CT equivalents over the unstable range of VCSRs, primarily due to the onset of dilatancy as failure approaches, as discussed earlier. The threshold VCSRs applying to the shallow-weathered CT-II samples again appear lower than for the deep CT-I cases. As with the earlier strain development plots, comparative trends are shown from CT tests performed on (low OCR and low K_0) Wenzhou clay (Guo et al. 2018) in Fig. 17(c) for comparison. The Wenzhou and Gault clays share broadly similar Δr_u^p evolutionary trends. However, the softer, younger clay is more susceptible to pore pressure accumulation at lower VCSRs than the stiff, heavily over-consolidated Gault clay.

Brosse (2012) and Brosse et al. (2017a) investigated the Gault clay's strength anisotropy through triaxial compression and extension and HCA tests run at Imperial College in London. The HCA tests on nominally identical rotary samples from 9.5 to 12.5 m depth, consolidated to in-situ K_0 stress conditions, were taken to undrained failure with specified σ_1 axis orientations α ranging from 0 to 90°, while maintaining b = 0.5 to give nominally plane strain conditions; triaxial compression and extension tests were conducted in parallel. The results identified significant effects of b value, or Lode angle, on the peak undrained shear strength (S_u) as well as mild anisotropy. More marked anisotropy was found in the maximum effective stress ratio (t/s') and mobilized ϕ'_{mob} (as assessed taking c' = 0), varying with α in monotonic HCA (b = 0.5) and triaxial (b = 0, 1) tests, as illustrated in Fig. 18. The effective stress conditions at which the three new undrained cyclic tests (reported in this paper) reached full failure first engaged their failure criteria are also plotted in Fig. 18 for comparison. Close correspondence can be seen for the two CHCA tests (106 and 108) confirming that cyclic failure develops when the pore pressures generated by repeated loading bring the specimens' stress states into contact with the Gault clay's anisotropic monotonic failure envelope. The single triaxial test CT-II (311) plots at a higher t/s' than expected, although this may be an accidental consequence of the various specimens' patterns of discontinuities.

Summary and conclusions

Series' of cyclic triaxial (CT) and hollow cylinder apparatus (CHCA) tests have been conducted on high-quality K_0–consolidated samples of intact (high OCR, high K_0) stiff Cretaceous (UK) Gault clay to explore their response to cyclic wheel loading. The CT tests involved vertical stress cycling, while the cardioid-shaped stress paths applied in the CHCA tests incorporated the principal stress rotation caused by wheel shear tractions. The permanent strain accumulation, resilient modulus degradation and pore pressure generation observed in the Gault clay experiments have been reported in detail, providing a unique dataset for geologically aged high OCR plastic stiff clays. Outcomes from Holocene soft clay from Wenzhou (SE China) conducted under identical cyclic loading conditions on specimens that were normally consolidated with K_0 = 0.55 in an earlier program have been shown to help to identify the distinctly different responses observed in the Gault clay. The following conclusions are drawn from the experiments:

1. The cyclic experiments indicated ranges of permanent strain, stiffness degradation and pore pressure response that could be classified as fully stable, metastable or unstable.
2. Principal stress rotation (PSR), which is implicit in wheel-loading, led to cyclic loading having a greater impact under metastable or unstable conditions at given vertical cyclic ratios (VCSRs) than in cyclic triaxial tests. PSR also led to the undesired impacts of cyclic loading appearing at VCSR thresholds that reduced as the PSR parameter η increased from zero (in CT tests) to 1/3 and 1/2 in the CHCA experiments.
3. High OCR, stiff Gault clay shows greater resistance to undrained CT and CHCA loading than the soft, low OCR Wenzhou clay. In addition, metastable and unstable CHCA tests conducted from K_0 = 1.8 consolidation conditions on the stiff clay led to extensive permanent axial strains developing, rather than the compressive straining seen in CT experiments and in both types of cyclic test on the soft, low K_0 Wenzhou clay.
4. Very significant excess pore pressures developed in metastable and unstable CT and CHCA tests that would be free to dissipate under roads or railways and so generate compressive volume strains and therefore surface settlements.
5. The stiffness responses seen in the cyclic tests run on Gault clay at ZJUT were shown to be fully compatible with high resolution measurements undertaken at ICL in triaxial and hollow cylinder tests which established the Gault clay's stiffness

and shear strength anisotropy under monotonic conditions in different triaxial and hollow cylinder apparatus.

6. The effective stress t/s', b and α conditions at which failures occurred in three of the 28 cyclic tests were also compatible with the outcomes of the earlier monotonic experiments. The cyclic tests confirmed that Gault clay features a brittle process with shear bands forming within which residual clay fabrics form that offer very low angles of shearing resistance. The brittleness can impact foundation and slope stability and calls for caution in practical engineering design.

The cyclic laboratory experiments undertaken on Gault clay help to identify the limiting conditions under which fully stable or metastable responses can be expected and so aid the optimal design or pavement or railway foundations and drainage systems to resist the development of excessive ground movements in service. Further studies are required on how long-term consolidation of cyclic pore pressures affects overall ground movements to complete the characterization of ground straining under wheel loading.

Data availability statement

Some or all data, models, and code that support the findings of this study are available from the corresponding author upon reasonable request.

Acknowledgements

The research described in this study was supported by Newton Advanced Fellowship from Royal Society of the UK (NA160438) and Natural Science Foundation of China (51761130078). The Authors are grateful to Dr Amandine Brosse (of GCG London) for providing data and plots from the earlier studies conducted at Imperial College, which were funded through the UK's Engineering and Physical Sciences Research Council under grant EP/D506387/1.

Notation

The following symbols are used in this paper:

b = intermediate principal stress ratio

d_i, d_o = inner and outer diameters of specimen

E_h^U, E_v^U = undrained Young's moduli for cross-anisotropic elastic soil

e_0 = initial void ratio

G_{vh} = shear modulus in vertical plane

$G_{z\theta}$ = shear resilient modulus

K_0 = coefficient of earth pressure

M_z^r = vertical resilient modulus

N = number of cycles

p', p'_0 = mean effective stress and initial mean effective stress, respectively

q = deviatoric stress

S_u = peak undrained shear strength

$s' = (\sigma'_1+\sigma'_3)/2$

$t = (\sigma'_1-\sigma'_3)/2$

u = pore water pressure

VCSR = vertical cyclic stress ratio

Y_2 = second yielding surface described by Jardine (1992)

α = orientation of major principal stress relative to vertical axis

$\gamma_{z\theta}$ = shear strain

$\gamma_{z\theta}^{p}$, $\gamma_{z\theta}^{r}$, $\gamma_{z\theta}^{t}$ = permanent, resilient, and total shear strains

Δr_u, Δr_u^{p} = pore pressure ratio and permanent pore pressure ratio, respectively

$\Delta\sigma'_z$, $\Delta\tau_{z\theta}$ = maximum increments of vertical cyclic stress and torsional shear stress

ε_1, ε_2, ε_3 = major, intermediate, and minor principal strains

ε_z, ε_r, ε_θ = vertical, radial, and circumferential strains

ε_z^{p}, ε_z^{r}, ε_z^{t} = permanent, resilient, and total vertical strains

η = ratio between shear stress and vertical cyclic stress

σ_1, σ_2, σ_3 = major, intermediate, and minor principal stresses

σ'_1, σ'_2, σ'_3 = major, intermediate, and minor effective principal stresses

σ_z, σ_r, σ_θ = vertical, radial, and circumferential stresses

σ'_z, σ'_θ = vertical and circumferential effective stresses

σ'_{z0}, σ'_{r0} = initial vertical and radial stresses

$\sigma_z^{\prime cyc}$, $\tau_{z\theta}^{cyc}$ = cyclic vertical and shear stresses

$\tau_{z\theta}$ = torsional shear stress

ϕ'_{mob} = mobilized shear angle

References

Aghakouchak, A., Sim, W. W. and Jardine, R. J. 2015. “Stress-path laboratory tests to characterise the cyclic behaviour of piles driven in sands.” *Soils Found.*, 55 (5): 917–928.

Brosse, A. M. 2012. “Study of the anisotropy of three British mudrocks using a hollow cylinder apparatus.” Ph.D. thesis, Imperial College London, London, UK.

Brosse, A. M., Jardine, R. J., and Nishimura, S. 2017a. “The undrained shear strength anisotropy of four Jurassic to Eocene stiff clays.” *Géotechnique*, 67 (8): 653–671.

Brosse, A. M., Hosseini Kamal, R., Jardine, R. J., and Coop, M. R. 2017b. “The shear stiffness characteristics of four Eocene-to-Jurassic UK stiff clays.” *Géotechnique*, 67 (3): 242–259.

Brown, S. F. 1996. “Soil mechanics in pavement engineering.” *Géotechnique*, 46 (3): 383–426.

Cai, Y. Q., Guo, L., Jardine, R. J., Yang, Z. X., and Wang, J. 2017. “Stress-strain response of soft clay to traffic loading.” *Géotechnique*, 67 (5): 446–451.

Cai, Y. Q., Sun, Q., Guo, L., Juang, C. H., and Wang, J. 2015. “Permanent deformation characteristics of saturated sand under cyclic loading.” *Can. Geotech. J.*, 52 (6): 795–807.

Chai, J. C., and Miura, N. 2002. “Traffic-load-induced permanent deformation of road on soft subsoil.” *J. Geotech. Geoenviron. Eng.*, 128 (11): 907–916.

Gräbe, P. J., and Clayton, C. R. I. 2009. “Effects of principal stress rotation on permanent deformation in rail track foundations." *J. Geotech. Geoenviron. Eng.*, 135 (4): 555–565.

Gräbe, P. J., and Clayton, C. R. I. 2014. "Effects of principal stress rotation on resilient behavior in rail track foundations." *J. Geotech. Geoenviron. Eng.*, 140 (2): 1–10.

Gu, C., Wang, J., Cai, Y. Q., Yang, Z. X., and Gao, Y. F. 2012. "Undrained cyclic triaxial behavior of saturated clays under variable confining pressure." *Soil Dyn. Earthq. Eng.*, 40: 118–128.

Guo, L., Cai, Y. Q., Jardine, R. J., Yang, Z. X., and Wang, J. 2018. "Undrained behaviour of intact soft clay under cyclic paths that match vehicle loading conditions." *Can. Geotech. J.*, 55 (1): 90–106.

Guo, L., Wang, J., Cai, Y. Q., Liu, H. L., Gao, Y. F., and Sun, H. L. 2013. "Undrained deformation behavior of saturated soft clay under long-term cyclic loading." *Soil Dyn. Earthq. Eng.*, 50: 28–37.

Hight, D. W., Gens, A., and Symes, M. J. 1983. "The development of a new hollow cylinder apparatus for investigating the effects of principal stress rotation in soils." *Géotechnique*, 33 (4): 355–383.

Hosseini Kamal, R. 2012. "Experimental study of the geotechnical properties of UK mudrocks." Ph.D. thesis, Imperial College London, London, UK.

Hosseini Kamal, R., Coop, M. R., Jardine, R. J., and Brosse, A. 2014. "The post-yield behaviour of four Eocene-to-Jurassic UK stiff clays." *Géotechnique*, 64 (8): 620–634.

Hyde, A. F. L., and Brown, S. F. 1976. “The plastic deformation of a silty clay under creep and repeated loading.” *Géotechnique*, 26 (1): 173–184.

Ishihara, K. 1996. *Soil behavior in earthquake geotechnics.* Oxford, UK: Clarendon Press.

Ishikawa, T., Sekine, E., and Miura, S. 2011. “Cyclic deformation of granular material subjected to moving-wheel loads.” *Can. Geotech. J.*, 48 (5): 691–703.

Jardine, R. J. 1992. “Observations on the kinematic nature of soil stiffness at small strains.” *Soils Found.*, 32 (2): 111–124.

Jardine, R. J., and Menkiti, C. O. 1999. “The undrained anisotropy of K0 consolidated sediments.” *In Proc. 12th ECSMGE, Amsterdam.* Vol. 2, Balkema, Rotterdam, pp. 1101–1108.

Lekarp, F., Isacsson, U., and Dawson, A. 2000. “State of the art. I: Resilient response of unbound aggregates.” *J. Transp. Eng.*, 126 (1): 66–75.

Li, D. Q., and Selig, E. T. 1996. “Cumulative plastic deformation for fine-grained subgrade soils.” *J. Geotech. Eng.*, 122 (12): 1006–1013.

Monismith, C. L., Ogawa, N., and Freeme, C. R. 1975. “Permanent deformation characteristics of subgrade soils due to repeated loading.” *Transportation Research Record. 537*, Transportation Research Board, Washington, D.C., 1–17.

Nakata, Y., Hyodo, M., Murata, H., and Yasufuku, N. 1998. “Flow deformation of sands subjected to principal stress rotation.” *Soils Found.*, 38 (2): 115–128.

Nishimura, S. 2006. “Laboratory study of the anisotropy of natural London clay.” Ph.D. thesis, Imperial College London, London, UK.

Nishimura, S., Minh, N. A., and Jardine, R. J. 2007. “Shear strength anisotropy of natural London clay.” *Géotechnique*, 57 (1): 49–62.

Powrie, W., Yang, L. A., and Clayton, C. R. I. 2007. “Stress changes in the ground below ballasted railway track during train passage.” *Proceedings of the Institution of Mechanical Engineers, Part F: Journal of Rail and Rapid Transit*, 221 (2): 247–261.

Puppala, A. J., Mohammad, L. N., and Allen, A. 1999. “Permanent deformation characterization of subgrade soils from RLT test.” *J. Mater. Civil Eng.*, 11 (4): 274–282.

Puppala, A. J., Saride, S., and Chomtid, S. 2009. “Experimental and modeling studies of permanent strains of subgrade soils.” *J. Geotech. Geoenviron. Eng.*, 135 (10): 1379–1389.

Qian, J. G., Du, Z. B., Lu, X. L., Gu, X. Q., and Huang, M. S. 2019. “Effects of principal stress rotation on stress–strain behaviors of saturated clay under traffic–load–induced stress path.” *Soils Found.*, 59 (1): 41–55.

Qian, J. G., Du, Z. B., and Yin, Z. Y. 2018. “Cyclic degradation and non-coaxiality of soft clay subjected to pure rotation of principal stress directions.” Acta Geotech., 13 (4): 943–959.

Shahu, J. T., Yudhbir, and Rao, N. S. V. K. 1999. “A simple test methodology for soils under transportation routes.” *Géotechnique*, 49 (5): 639–649.

Suiker, A. S., Selig, E. T., and Frenkel, R. 2005. “Static and Cyclic Triaxial Testing of Ballast and Subballast.” *J. Geotech. Geoenviron. Eng.*, 131 (6): 771–782.

Towhata, I., and Ishihara, K. 1985. "Undrained strength of sand undergoing cyclic rotation of principal stress axes." *Soils Found.*, 25 (2): 135–147.

Wang, J., Guo, L., Cai, Y. Q., Xu, C. J., and Gu, C. 2013. "Strain and pore pressure development on soft marine clay in triaxial tests with a large number of cycles." *Ocean Eng.*, 74 (1): 125–132.

Wilkinson, S. 2011. "The microstructure of UK mudrocks." Ph.D. thesis, Imperial College London, London, UK.

Wu, T. Y., Cai, Y. Q., Guo, L., Ling, D. S., and Wang, J. 2017. "Influence of shear stress level on cyclic deformation behaviour of intact Wenzhou soft clay under traffic loading." *Eng. Geol.*, 228: 61–70.

Xiao, J. H., Juang, C. H., Wei, K., and Xu, S. Q. 2014. "Effects of principal stress rotation on the cumulative deformation of normally consolidated soft clay under subway traffic loading." *J. Geotech. Geoenviron. Eng.*, 140 (4): 04013046.

Yang, Z. X., Li, X. S., and Yang, J. 2007. "Undrained anisotropy and rotational shear in granular soil." *Géotechnique*, 57 (4): 371–384.

Yasuhara, K., Yamanouchi, T., and Hirao, K. 1982. "Cyclic strength and deformation of normally consolidated clay." *Soils Found.*, 22 (3): 77–91.

Zdravkovic, L., and Jardine, R.J. 1997. "Some anisotropic stiffness characteristics of a silt under general stress conditions." *Géotechnique*, 47 (3): 407–437

Zhou, J., and Gong, X. N. 2001. "Strain degradation of saturated clay under cyclic loading." *Can. Geotech. J.*, 38 (1): 208–212.

Figure captions

Fig. 1. (a) Deviatoric stress and (b) pore pressure versus axial strain for Gault clay in triaxial compression; redrawn from Hosseini Kamal (2012)

Fig. 2. Schematic of the re-consolidation to in-situ stresses

Fig. 3. Example of stress conditions in CHCA test with VCSR = 0.127; (a) cyclic stresses versus elapsed time; (b) incremental stress paths

Fig. 4. Typical (a) vertical and (b) shear stress-strain hysteresis loops in a single cycle

Fig. 5. Vertical strain evolutions of deep samples in CT-I tests

Fig. 6. Vertical strain evolutions of deep samples in CHCA tests with η = 1/3

Fig. 7. Comparison between CT-I and CHCA tests in vertical strain

Fig. 8. Permanent vertical strain after different cycles versus VCSR: (a) CHCA series with η = 1/3; (b) CT-I series; (c) CT-II series

Fig. 9. Permanent shear strain after different cycles versus VCSR in CHCA tests with η = 1/3

Fig. 10. Typical hysteretic responses in CT-I and CHCA tests with VCSR = 0.343

Fig. 11. Vertical hysteresis loops at different cycles in CT-I and CHCA tests with VCSR = 0.343

Fig. 12. Variation of normalized resilient modulus with N in three series tests: (a) CHCA tests (η = 1/3); (b) CT-I tests; (c) CT-II tests

Fig. 13. Typical shear stress-strain hysteresis loops in CHCA tests

Fig. 14. Variation of $G_{z\theta}$ with N in CHCA tests

Fig. 15. Pore pressure generation of deep samples in CT-I tests

Fig. 16. Pore pressure generation of deep samples in CHCA tests with η = 1/3

Fig. 17. Permanent pore pressure after different cycles versus VCSR: (a) CHCA series with η = 1/3; (b) CT-I series; (c) CT-II series

Fig. 18. Variations of maximum stress ratio t/s' with the orientation of major principle stress α covering both the monotonic and cyclic shear tests

Table 1. Index properties of tested Gault clay

Index property	Shallow-weathered samples	Deep samples
Specific gravity, G_s	2.59	2.59
Initial density, ρ_0 (g/cm^3)	1.92-1.97	1.95-2.02
Natural water content, w_n (%)	28-30	26-29
Plastic limit, w_p (%)	24	25
Liquid limit, w_l (%)	65	67
Plasticity index, I_P	41	42
Clay fraction (%)	60-63	60-63
Undrained shear strength[a], S_u (kPa)	≈70	≈120

[a] after Hosseini Kamal (2012)

Table 2. Summary of compression and strength parameters of Gault clay; after Hosseini Kamal et al. (2014)

Parameter	Value
Location of intrinsic normal compression line, N^*	2.99
Location of intrinsic critical state line, Γ^*	2.85
Gradient of intrinsic normal compression line, λ^*	0.215
Gradient of intrinsic swelling line, κ^*	0.04
Intrinsic compression index, C_c^*	0.496
Intrinsic swelling index, C_s^*	0.168
Intact compression index, C_c	0.221
Intact swelling index, C_s	0.095
Ratio of swell sensitivity, C_s^*/C_s	1.77
Critical state angle of shearing resistance, ϕ'_{cs}	24.8°
Residual angle of shearing resistance, ϕ'_r	10°

* effective stress parameters applying to reconstituted clay

Table 3. Measurement ranges and resolutions of transducers in DYNHCA

Transducer	Measurement range	Resolution
Vertical load cell	0-3 kN	0.3 N
Torque transducer	0-30 Nm	0.03 Nm
Vertical displacement transducer	0-93 mm	0.0002 mm
Rotating angle transducer	Without restriction	0.0011°
Pressure transducers (inner/outer cell pressure & back pressure)	0-2 MPa	0.5 kPa
Volume change transducers (inner/outer cell pressure & back pressure)	0-200 cm^3	1 mm^3
Pore water pressure transducer	0-1 MPa	0.5 kPa

Table 4. Equations of stresses and strains in a CHCA; after Yang et al. (2007)

	Stresses	Strains
Vertical	$\sigma_z = \frac{W}{\pi(r_o^2 - r_i^2)} + \frac{p_o r_o^2 - p_i r_i^2}{(r_o^2 - r_i^2)}$	$\varepsilon_z = -\frac{\Delta H}{H}$
Radial	$\sigma_r = \frac{p_o r_o + p_i r_i}{r_o + r_i}$	$\varepsilon_r = -\frac{\Delta r_o - \Delta r_i}{r_o - r_i}$
Circumferential	$\sigma_\theta = \frac{p_o r_o - p_i r_i}{r_o - r_i}$	$\varepsilon_\theta = -\frac{\Delta r_o + \Delta r_i}{r_o + r_i}$
Shear	$\tau_{z\theta} = \frac{3T}{2\pi(r_o^3 - r_i^3)}$	$\gamma_{z\theta} = \frac{2\Delta\theta(r_o^3 - r_i^3)}{3H(r_o^2 - r_i^2)}$
Major principal	$\sigma_1 = \frac{\sigma_z + \sigma_\theta}{2} + \sqrt{(\frac{\sigma_z - \sigma_\theta}{2})^2 + (\tau_{z\theta})^2}$	$\varepsilon_1 = \frac{\varepsilon_z + \varepsilon_\theta}{2} + \sqrt{(\frac{\varepsilon_z - \varepsilon_\theta}{2})^2 + (\frac{\gamma_{z\theta}}{2})^2}$
Intermediate principal	$\sigma_2 = \sigma_r$	$\varepsilon_2 = \varepsilon_r$
Minor principal	$\sigma_3 = \frac{\sigma_z + \sigma_\theta}{2} - \sqrt{(\frac{\sigma_z - \sigma_\theta}{2})^2 + (\tau_{z\theta})^2}$	$\varepsilon_3 = \frac{\varepsilon_z + \varepsilon_\theta}{2} - \sqrt{(\frac{\varepsilon_z - \varepsilon_\theta}{2})^2 + (\frac{\gamma_{z\theta}}{2})^2}$

Note: *H*, initial specimen height; r_i and r_o, inner and outer radii; ΔH, vertical displacement; Δr_i and Δr_o, inner and outer radial displacements; $\Delta\theta$ = relative torsional angle between the specimen top and bottom; p_i and p_o, inner and outer cell pressures; *W*, vertical load; *T*, torque.

Table 5. Summary of three series of cyclic tests for Gault clay

Series	Sample type	Depth (m)	e_0	$\Delta\sigma'_z$ (kPa)	$\Delta\tau_{z\theta}$ (kPa)	VCSR	η	N	Test ID
CHCA	Deep	7.38	0.77	15.9	5.3	0.067	1/3	50000	101
	(σ'_{z0} = 77 kPa	5.66	0.80	30	10	0.127	1/3	50000	102
	σ'_{r0} = 139 kPa)	5.41	0.71	53.1	17.7	0.225	1/3	50000	103
		7.74	0.72	67.5	22.5	0.286	1/3	50000	104
		7.99	0.73	81	27	0.343	1/3	50000	105
		5.91	0.83	81	40.5	0.343	1/2	2460	106
		8.30	0.74	94.5	31.5	0.400	1/3	50000	107
		7.01	0.80	106.2	35.4	0.450	1/3	5020	108
CT-I	Deep	7.01	0.79	15.9	0	0.067	0	50000	201
	(σ'_{z0} = 77 kPa	7.01	0.79	21	0	0.088	0	50000	202
	σ'_{r0} = 139 kPa)	7.01	0.80	30	0	0.127	0	50000	203
		7.38	0.77	60.5	0	0.256	0	50000	204
		8.30	0.74	81	0	0.343	0	50000	205
		7.38	0.77	88.5	0	0.375	0	50000	206
		7.38	0.77	118.5	0	0.502	0	50000	207
		8.30	0.74	141.6	0	0.600	0	50000	208
		8.30	0.73	165	0	0.699	0	50000	209
CT-II	Shallow-	3	0.76	10.5	0	0.088	0	10000	301
	weathered	3	0.80	19.8	0	0.165	0	10000	302
	(σ'_{z0} = 39 kPa	3	0.73	24.6	0	0.205	0	10000	303
	σ'_{r0} = 70 kPa)	3	0.72	29.4	0	0.245	0	10000	304
		3	0.73	34.3	0	0.286	0	10000	305
		3	0.69	36	0	0.300	0	10000	306
		3	0.79	48	0	0.400	0	10000	307
		3	0.80	54	0	0.450	0	10000	308
		3	0.72	66	0	0.550	0	10000	309
		3	0.73	78	0	0.650	0	10000	310
		3	0.76	96	0	0.800	0	2280	311

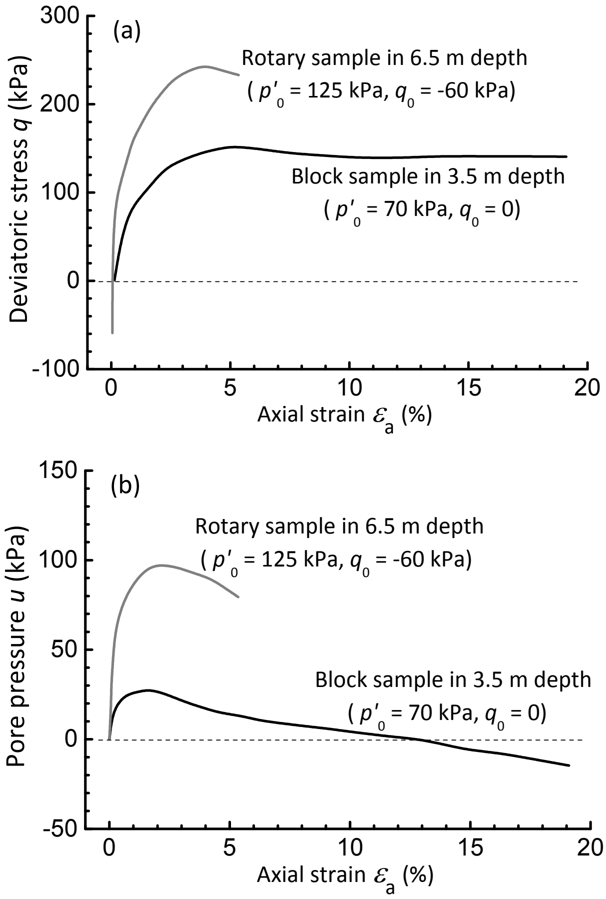

Fig. 1. (a) Deviatoric stress and (b) pore pressure versus axial strain for Gault clay in triaxial compression; redrawn from Hosseini Kamal (2012)

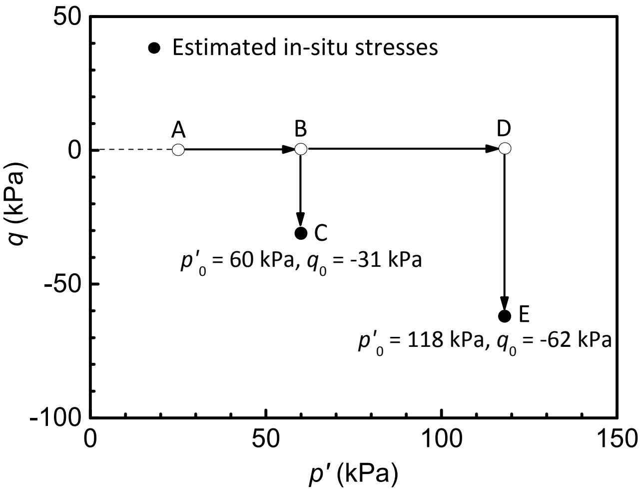

Fig. 2. Schematic of the re-consolidation to in-situ stresses

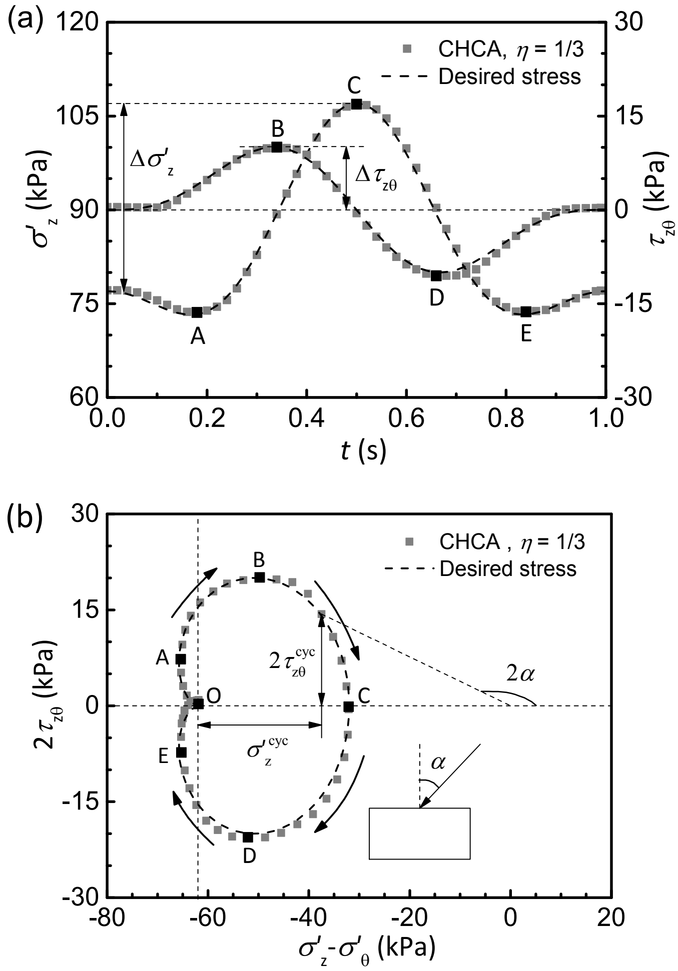

Fig. 3. Example of stress conditions in CHCA test with VCSR = 0.127; (a) cyclic stresses versus elapsed time; (b) incremental stress paths (Note: point O denotes state after K_0 consolidation)

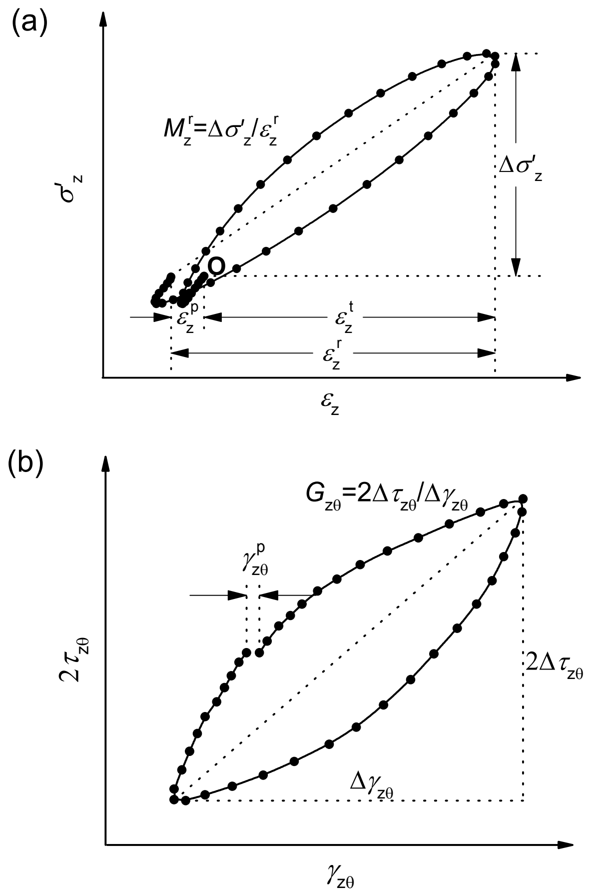

Fig. 4. Typical (a) vertical and (b) shear stress-strain hysteresis loops in a single cycle

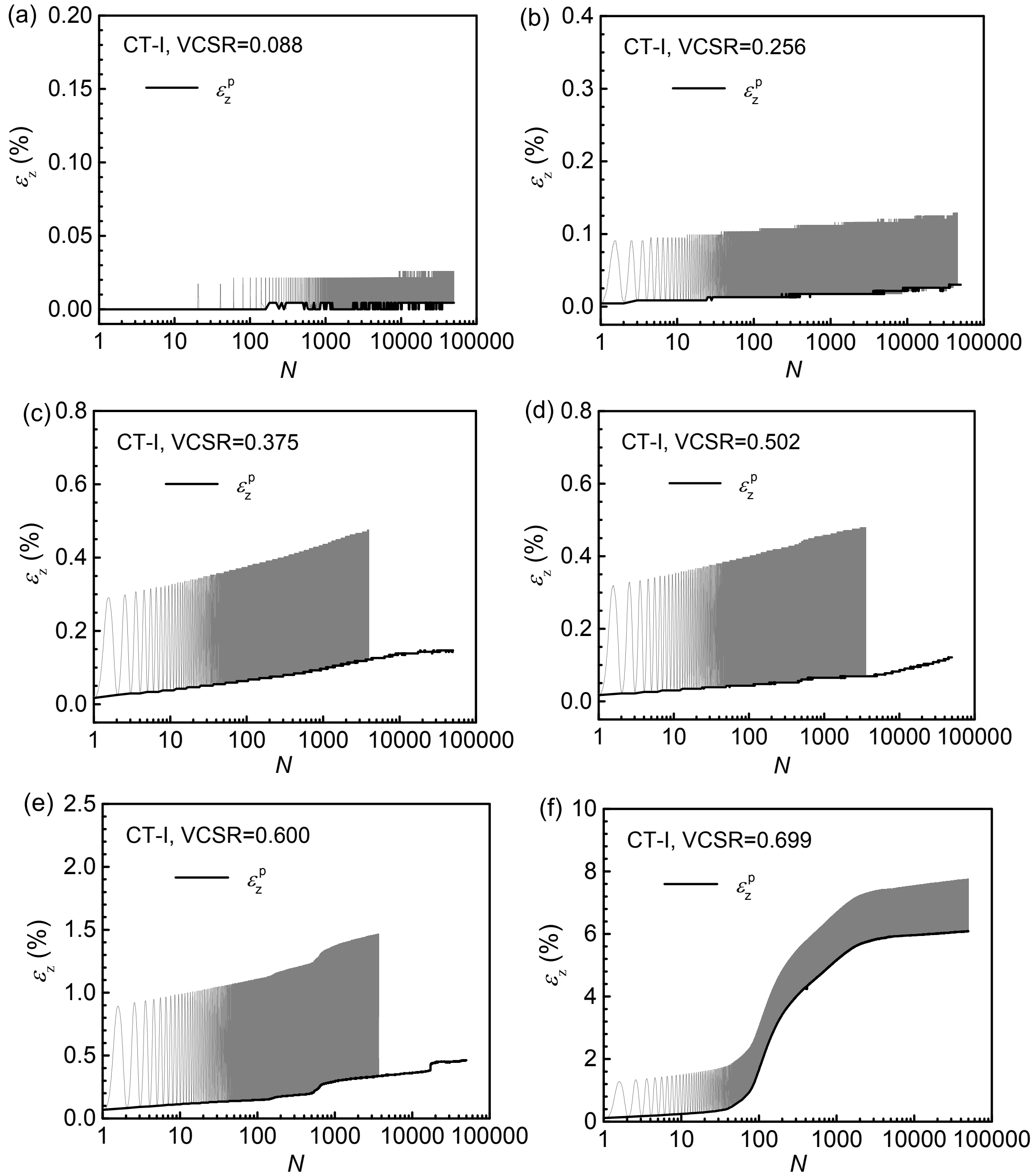

Fig. 5. Vertical strain evolutions of deep samples in CT-I tests: (a) VCSR = 0.088; (b) VCSR = 0.256; (c) VCSR = 0.375; (d) VCSR = 0.502; (e) VCSR = 0.600; (f) VCSR = 0.699

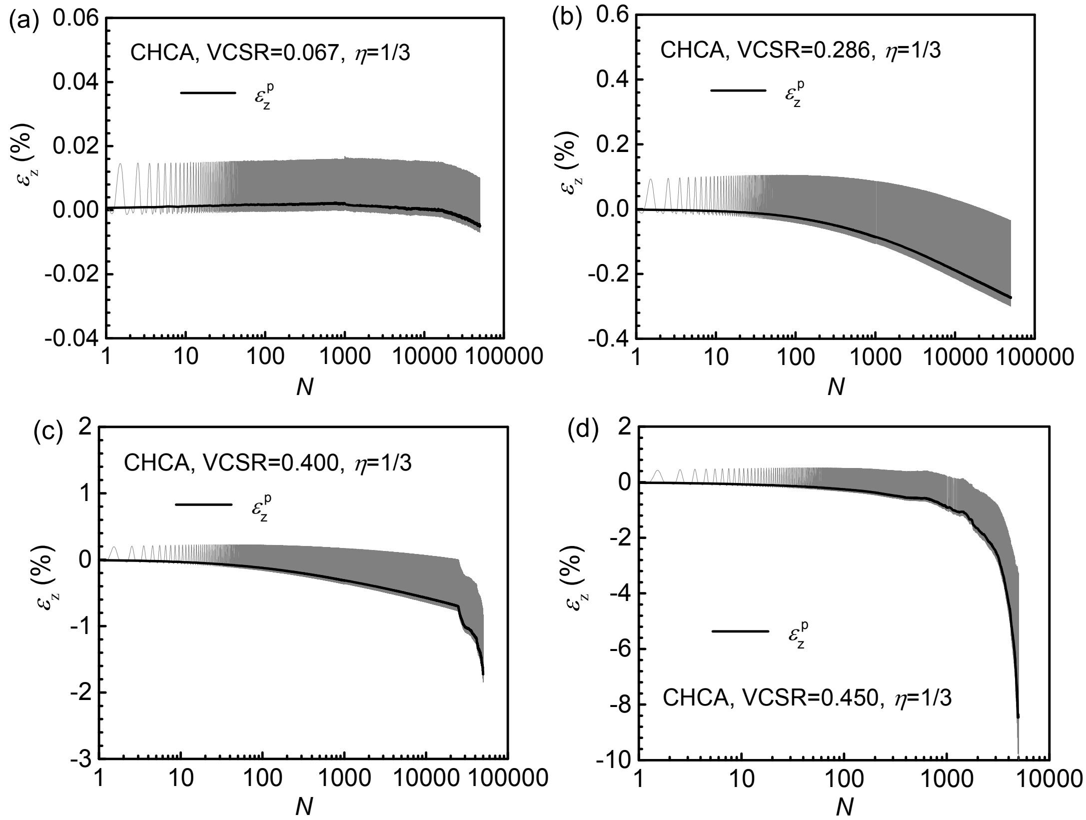

Fig. 6. Vertical strain evolutions of deep samples in CHCA tests with η = 1/3: (a) VCSR = 0.067; (b) VCSR = 0.286; (c) VCSR = 0.400; (d) VCSR = 0.450

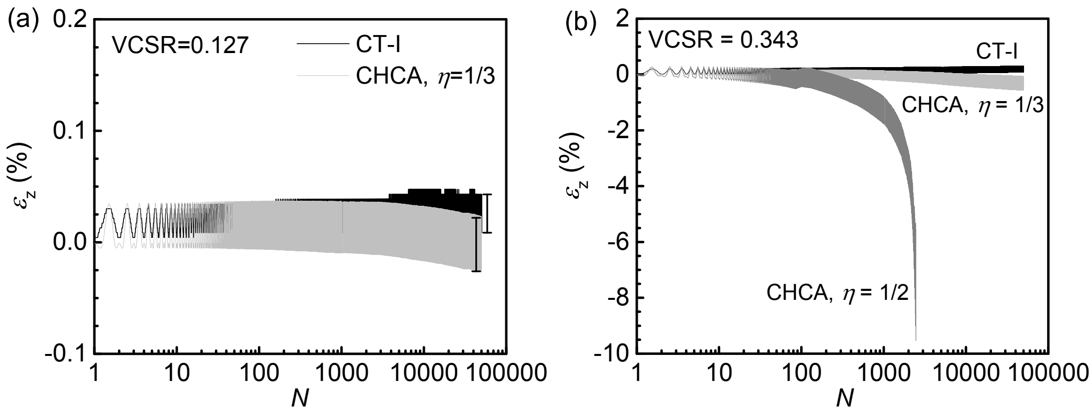

Fig. 7. Comparison between CT-I and CHCA tests in vertical strain: (a) VCSR = 0.127; (b) VCSR = 0.343

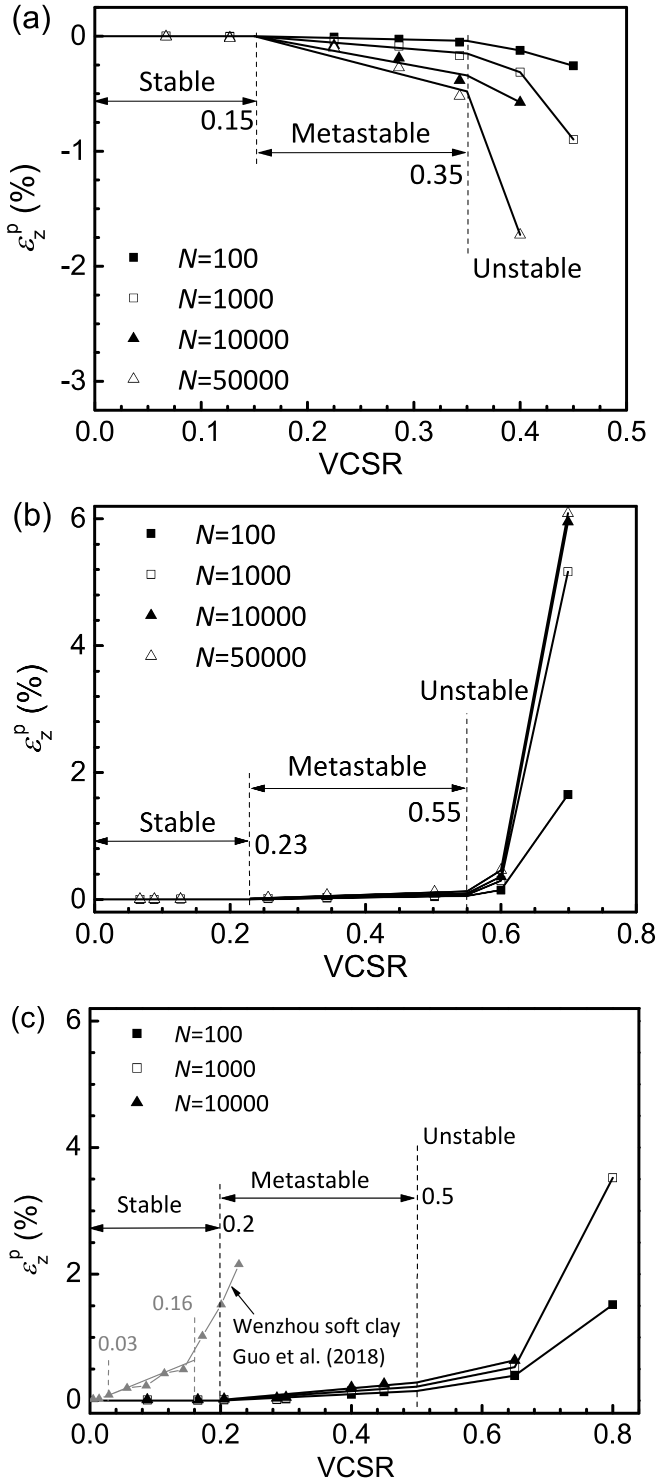

Fig. 8. Permanent vertical strain after different cycles versus VCSR: (a) CHCA series with η = 1/3; (b) CT-I series; (c) CT-II series

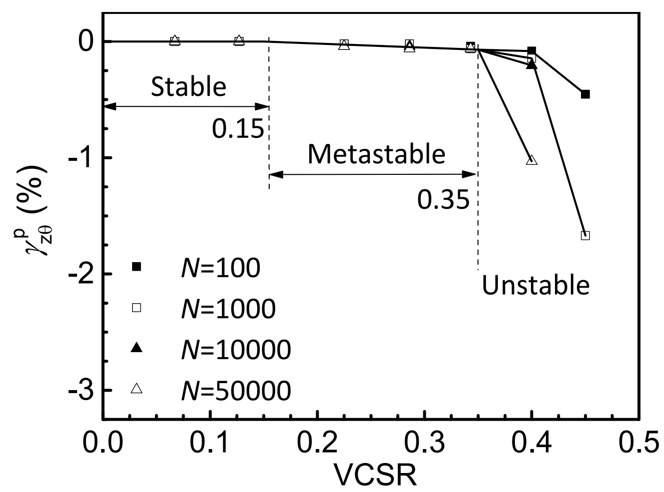

Fig. 9. Permanent shear strain after different cycles versus VCSR in CHCA tests with η = 1/3

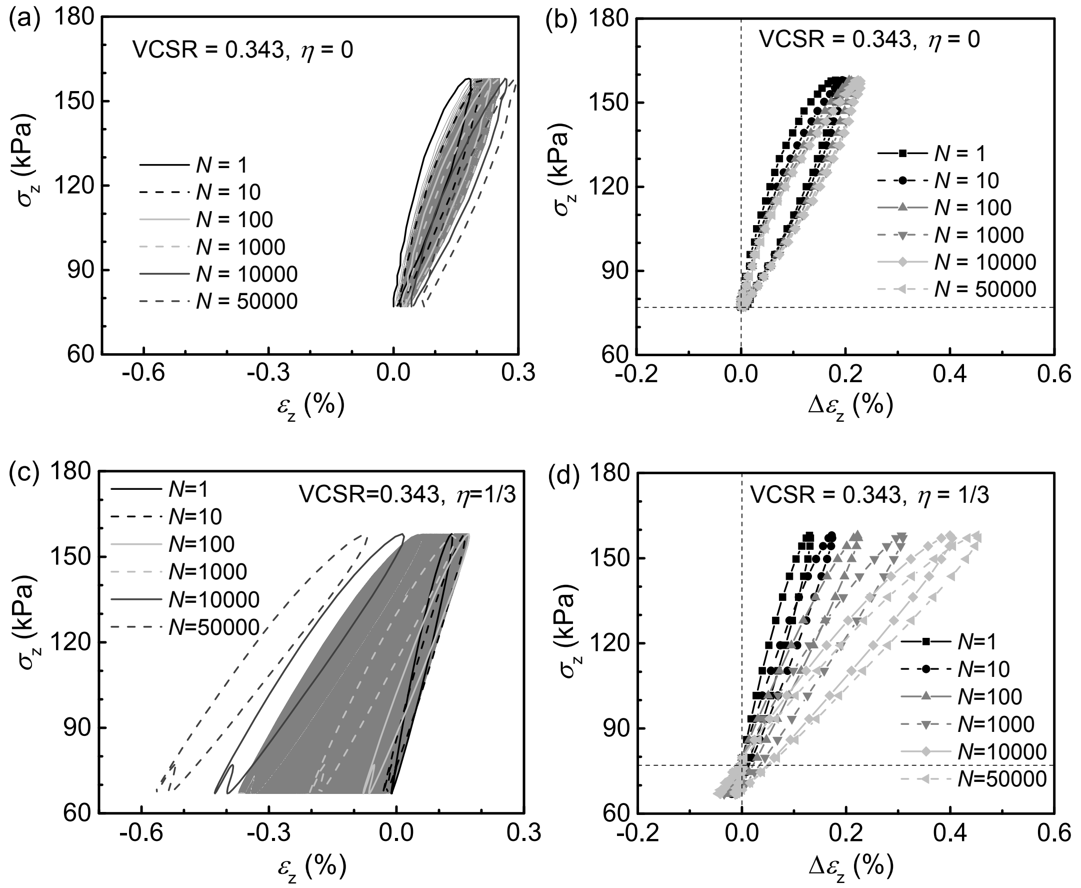

Fig. 10. Typical hysteretic responses in CT-I and CHCA tests with VCSR = 0.343: (a) and (c) complete vertical stress-strain loops; (b) and (d) vertical stress-strain loops at different cycles

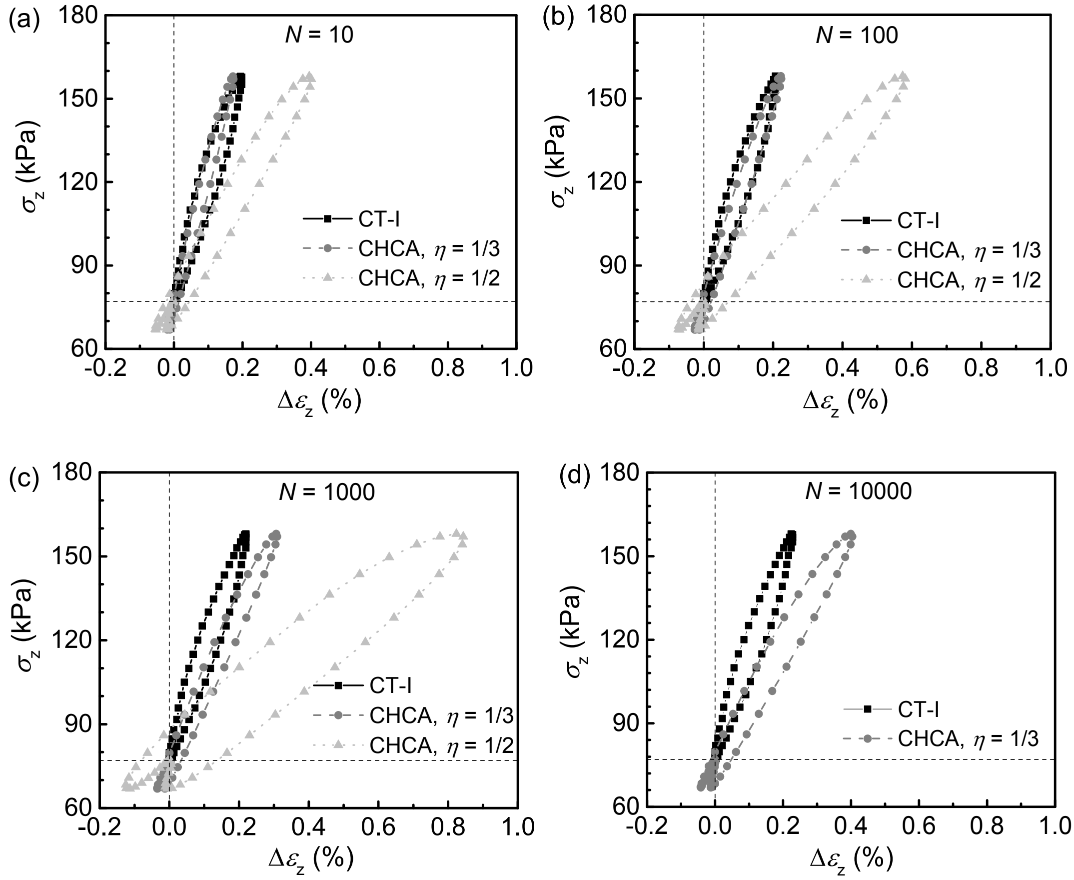

Fig. 11. Vertical hysteresis loops at different cycles in CT-I and CHCA tests with VCSR = 0.343: (a) N = 10; (b) N = 100; (c) N = 1000; (d) N = 10000

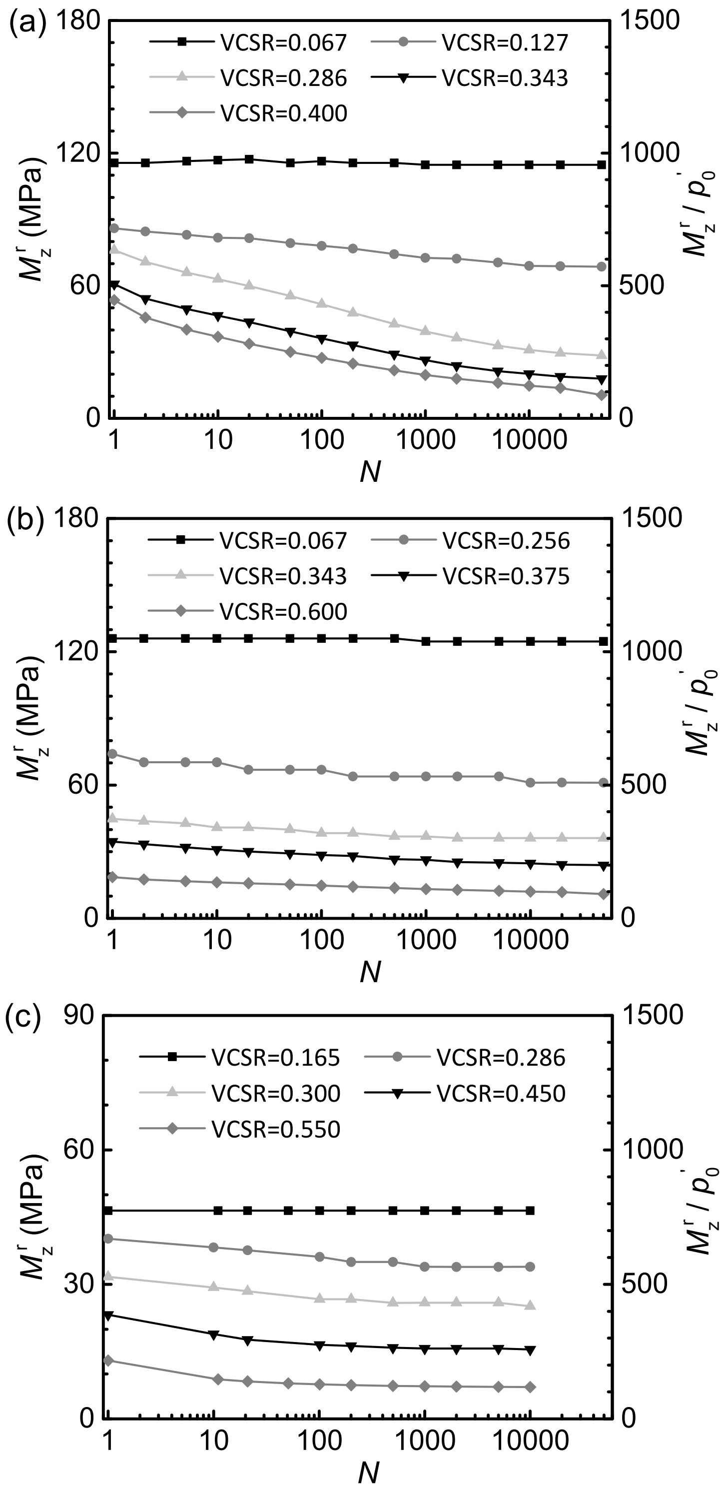

Fig. 12. Variation of normalized resilient modulus with *N* in three series tests: (a) CHCA tests (η = 1/3); (b) CT-I tests; (c) CT-II tests

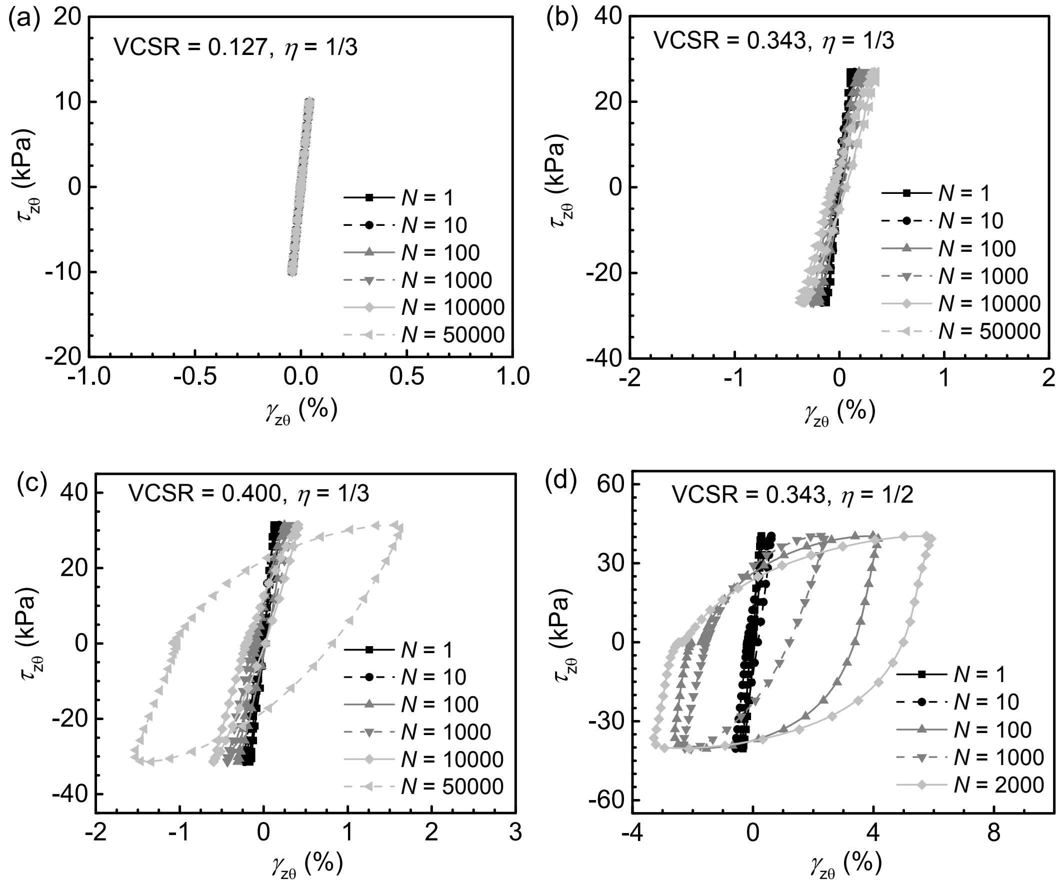

Fig. 13. Typical shear stress-strain hysteresis loops in CHCA tests: (a) VCSR = 0.127, η = 1/3; (b) VCSR = 0.343, η = 1/3; (c) VCSR = 0.400, η = 1/3; (d) VCSR = 0.343, η = 1/2

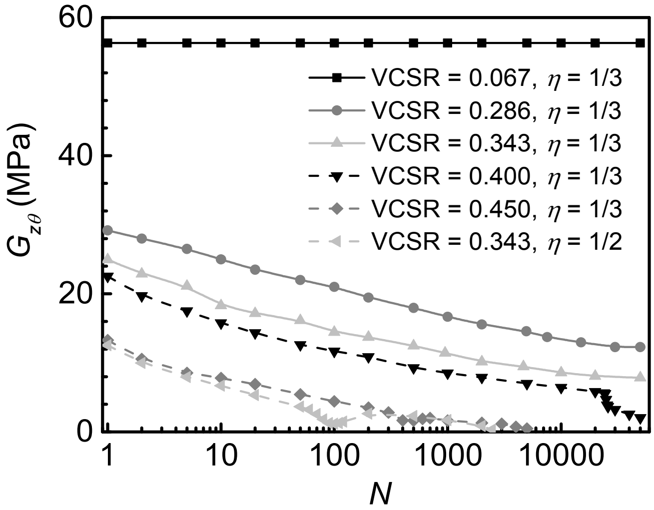

Fig. 14. Variation of $G_{z\theta}$ with N in CHCA tests

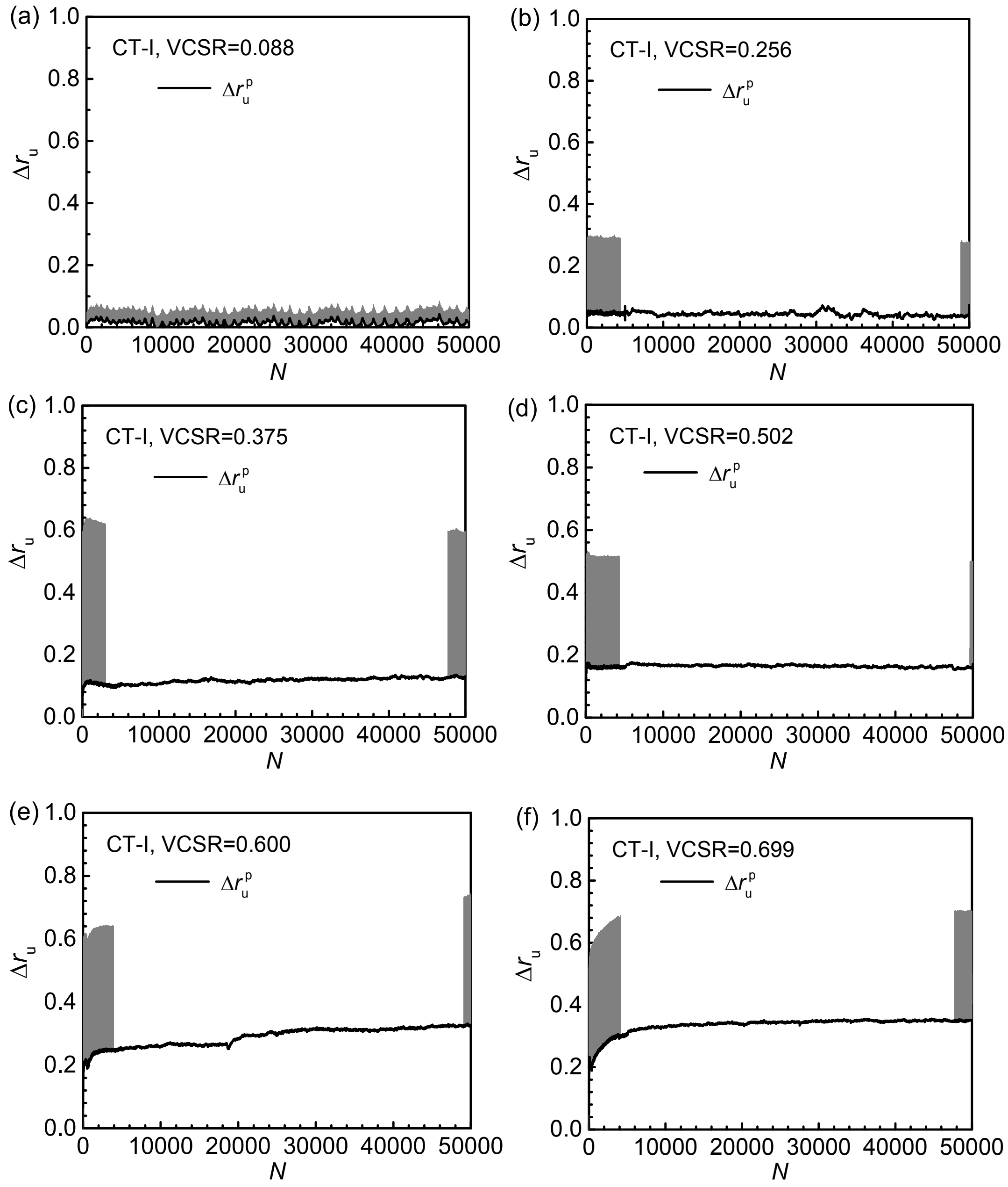

Fig. 15. Pore pressure generation of deep samples in CT-I tests: (a) VCSR = 0.088; (b) VCSR = 0.256; (c) VCSR = 0.375; (d) VCSR = 0.502; (e) VCSR = 0.600; (f) VCSR = 0.699

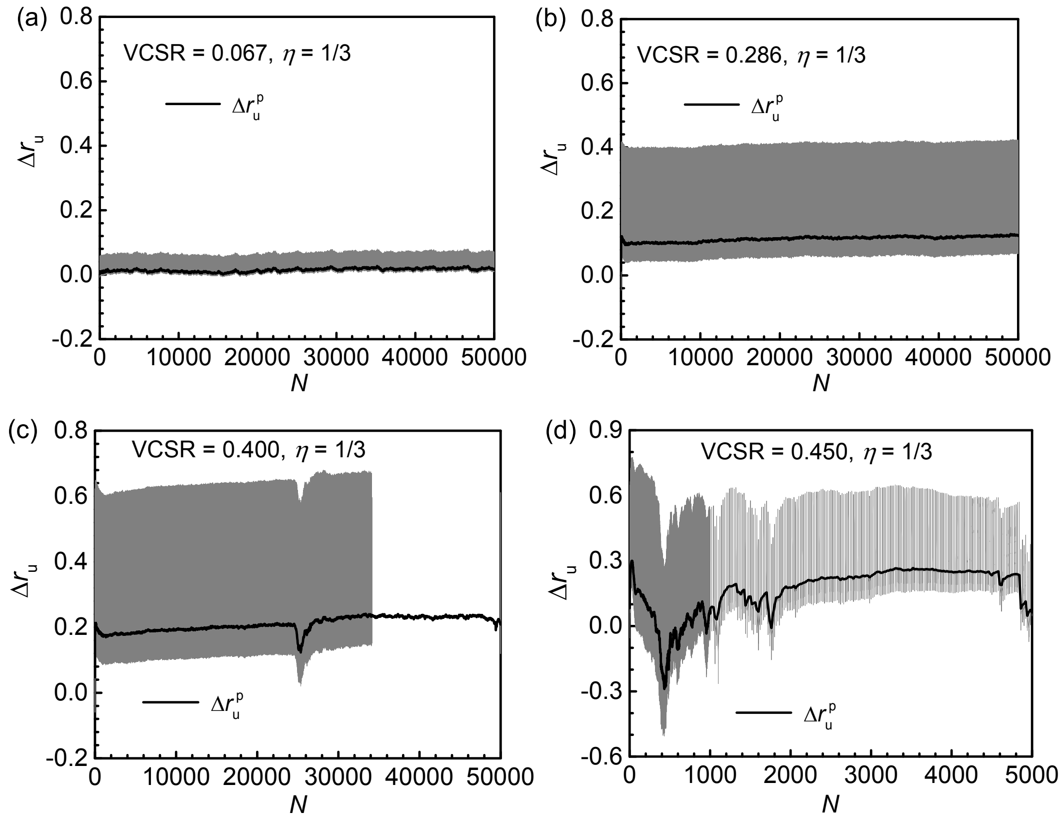

Fig. 16. Pore pressure generation of deep samples in CHCA tests with η = 1/3: (a) VCSR = 0.067; (b) VCSR = 0.286; (c) VCSR = 0.400; (d) VCSR = 0.450

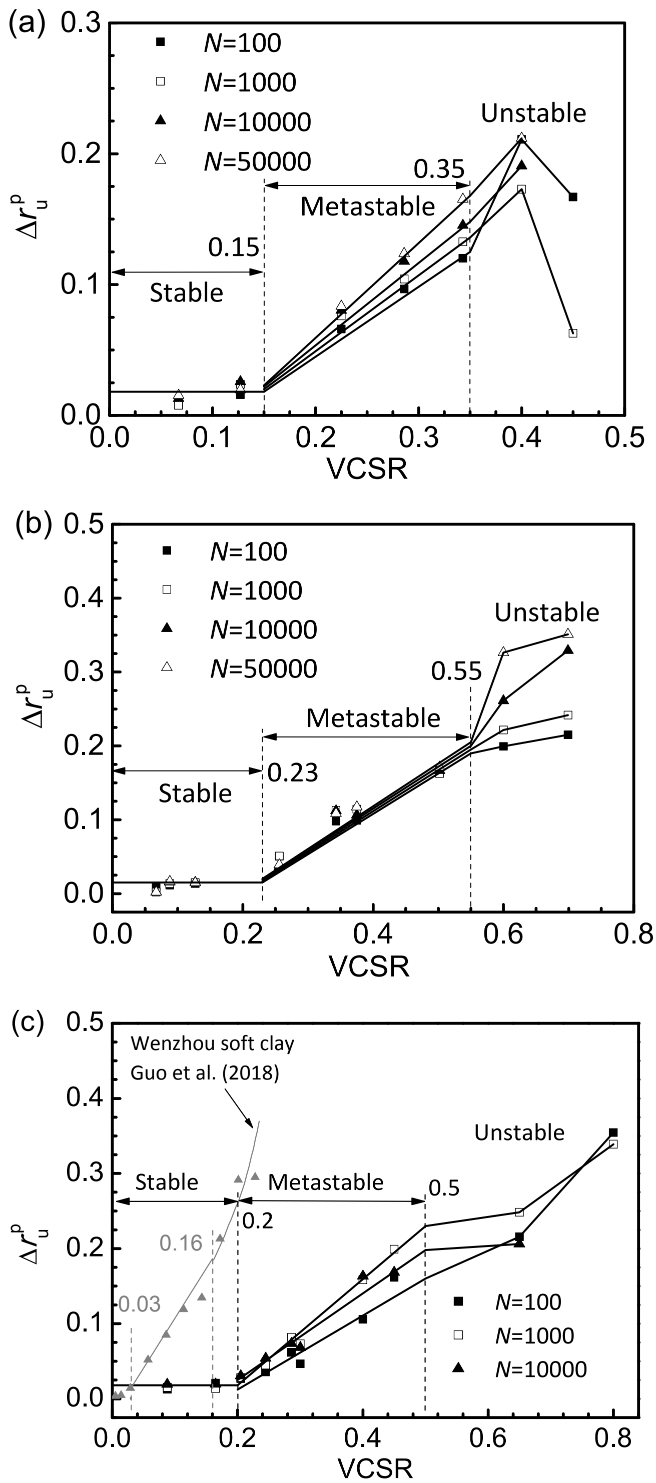

Fig. 17. Permanent pore pressure after different cycles versus VCSR: (a) CHCA series with η = 1/3; (b) CT-I series; (c) CT-II series

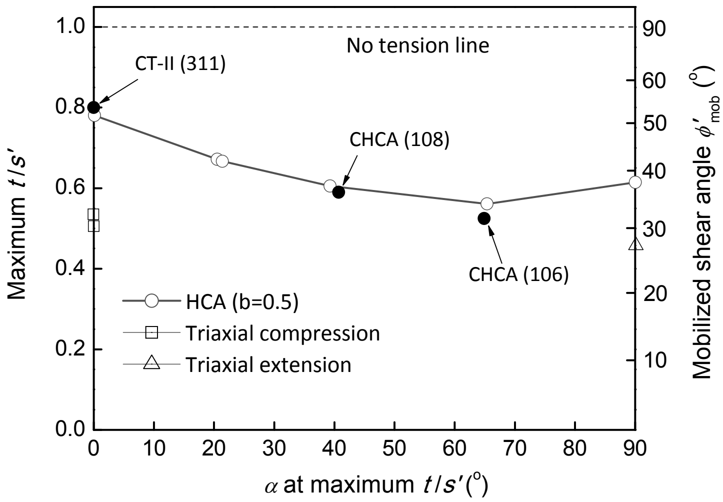

Fig. 18. Variations of maximum stress ratio *t/s'* with the orientation of major principle stress *α* covering both the monotonic and cyclic shear tests (Note: hollow symbols represent monotonic test data from Brosse (2012) and solid symbols represent cyclic test data from this study)